Microwave Imaging of Mixed Metallic–Dielectric Configurations via a Finite Element-Based Variable Exponent Approach

Valentina Schenone, Alessandro Fedeli, Claudio Estatico, Matteo Pastorino, and Andrea Randazzo

Abstract – The quantitative reconstruction of structures that include both metallic and dielectric targets at the same time is addressed in this article. In particular, a nonlinear tomographic inversion approach developed in variable exponent Lebesgue spaces with a finite element (FE) formulation is adopted for the first time in such a configuration. Results obtained within a simulated environment are presented to validate the proposed technique and analyze the effects of different numbers and sizes of the metallic targets present in the investigated scenario. Moreover, the impact of possible a priori knowledge of metallic structures is assessed.

1. Introduction

On several occasions, it could be practically useful to acquire quantitative microwave images of targets that contain mixed metallic–dielectric configurations. Such structures can be found in different contexts, ranging from medical diagnostics (e.g., limbs with prosthetic implants) to civil engineering (e.g., reinforced concrete) and geophysics (e.g., metals in ores). The presence of metallic parts does influence the distribution of fields significantly inside the region of interest and at antenna ports, and the composition with dielectric targets causes strong nonlinearities of the underlying electromagnetic inverse scattering problem to emerge [1].

Although microwave imaging of metallic structures has been considered for a long time and several interesting results can be found in the literature [2–5], most of the proposed approaches are qualitative or radar based [6–8]. Fewer research contributions are oriented to the quantitative inversion of configurations with both dielectric and metallic targets [9].

In this article, for the first time, a quantitative inverse scattering method framed in variable exponent Lebesgue spaces is considered for the reconstruction of mixed metallic–dielectric target configurations. The inverse scattering technique operates under two-dimensional hypotheses and features a finite element (FE)-based formulation, which is suitable to enforce boundary conditions at both metallic edges and antenna ports [10]. The method belongs to the class of the so-called inexact Newton (IN) iterative approaches, which are proven very effective in dealing with the nonlinearity of the inverse problem [11, 12]. Furthermore, it includes an adaptive selection of the exponent function defining the working $L^{p(\cdot)}$ spaces, refined on the basis of reconstruction results, iteration after iteration [13].

The proposed approach is validated with simulated test cases, in the presence of one or more metallic regions of different size and assuming the metallic parts either known or completely unknown to the inversion method, to evaluate the impact of possible a priori information. A brief overview of the solution procedure is outlined in the following, followed by a discussion about numerical results.

Manuscript received 27 December 2021.

Valentina Schenone, Alessandro Fedeli, Matteo Pastorino, and Andrea Randazzo are with the Department of Electrical, Electronic, Telecommunications Engineering and Naval Architecture, University of Genoa, via all'Opera Pia 11A, 16145 Genoa, Italy; e-mail: valentina.schenone@edu.unige.it, alessandro.fedeli@unige.it, matteo.pastorino@unige.it, andrea.randazzo@unige.it.

Claudio Estatico is with the Department of Mathematics, University of Genoa, via Dodecaneso 35, 16146 Genova, Italy; e-mail: estatico@dima.unige.it.

2. Inverse Scattering Approach

Let us consider a cylindrical target composed by both metallic and dielectric parts, whose cross-section is located inside a certain region of interest R. Such a target is surrounded by I antennas, which provide, excited one at a time, a time harmonic illuminating electromagnetic radiation at the angular frequency ω. The target is described by a contrast function $\tau(\mathbf{r}) = \varepsilon^*(\mathbf{r})/\varepsilon_0 - 1$, $\mathbf{r} = (x, y) \in R$, where $\varepsilon^*(\mathbf{r}) = \varepsilon(\mathbf{r}) - j\sigma(\mathbf{r})/\omega$, and ε and σ are the dielectric permittivity and electric conductivity, respectively, and ε_0 the permittivity of a vacuum. Transmission S parameters are measured for each view between couples of antenna ports i, j, skipping the L antennas closest to the source, with and without the target (i.e., total and incident S parameters, denoted as $S^{\text{tot}}_{i,j}$ and $S^{\text{inc}}_{i,j}$, $i \neq j$). Under the assumption of z-polarized transverse magnetic electromagnetic fields (i.e., polarized along the axis of cylindrical targets), the relationship between scattered S parameters $\Delta S_{i,j} = S^{\text{tot}}_{i,j} - S^{\text{inc}}_{i,j}$ and τ is given by

$$\Delta S_{i,j} = \mathcal{A}_{i,j}(\tau) \tag{1}$$

where the operator $\mathcal{A}_{i,j}$ is defined as

$$\mathcal{A}_{i,j}(\tau) = A_{i,j} \int_R \tau(\mathbf{r}') E^{\text{inc}}_i(\mathbf{r}') E^{\text{tot}}_{j\tau}(\mathbf{r}') d\mathbf{r}' \tag{2}$$

with $A_{i,j} = -j\omega\varepsilon_0 / (2a_i a_j)$, and a_i and a_j being the amplitudes of the incoming waves at ports i and j,

respectively [14]. In (2), E_m^{inc} and $E_{m\tau}^{\text{tot}}$ represent the z component of the incident and total electric fields when the mth antenna is acting in transmitting mode. For numerically solving (1) in the variable τ, the region R has been partitioned into N triangles R_n ($n = 1, \ldots, N$), assuming a constant value of τ in each element (i.e., $\tau(\mathbf{r}) = \tau_n$, $\mathbf{r} \in R_n$) and using triangular basis functions of the first order $\delta_q^n(\mathbf{r})$ to express internal fields (i.e., $E_m^l(\mathbf{r}) = \sum_{q=1}^{3} E_{m,q}^{l,n} \delta_q^n(\mathbf{r})$, $\mathbf{r} \in R_n$) [15]. Putting together all the available S-parameter data, we obtain the following system of equations:

$$\underbrace{\begin{bmatrix} A_{2+L,1} \sum_{n=1}^{N} \sum_{q=1}^{3} \sum_{w=1}^{3} \tau_n E_{2+L,q}^{\text{inc},n} E_{1\tau,w}^{\text{tot},n} Q_{q,w}^n \\ \vdots \\ A_{K,I} \sum_{n=1}^{N} \sum_{q=1}^{3} \sum_{w=1}^{3} \tau_n E_{K,q}^{\text{inc},n} E_{I\tau,w}^{\text{tot},n} Q_{q,w}^n \end{bmatrix}}_{\mathbf{A}(\boldsymbol{\tau})} = \underbrace{\begin{bmatrix} \Delta S_{2+L,1} \\ \vdots \\ \Delta S_{K,I} \end{bmatrix}}_{\mathbf{y}} \tag{3}$$

where $K = I - L - 1$, $Q_{q,w}^n = \int_{R_n} \delta_q^n \delta_w^n d\mathbf{r}'$, $\boldsymbol{\tau} = [\tau_1, \ldots, \tau_N]^t \in X$, and $\mathbf{y} \in Y$. Note that the operator $\mathbf{A}(\boldsymbol{\tau}) : X \to Y$ is nonlinear because each total field coefficient $E_{j\tau,w}^{\text{tot},n}$, in turn, depends on the contrast function τ in the whole R.

The solution of (3) is retrieved by an IN scheme, formulated considering X a variable exponent Lebesgue space $L^{p(\cdot)}$ [16], where its exponent function is in this case an array of discrete values $\mathbf{p} = [p_1, \ldots, p_N]^t$, one for each triangle of the mesh R_n. In more detail, the IN procedure iteratively linearizes (3) around the contrast function at each kth step $\boldsymbol{\tau}_{(k)} = \left[\tau_1^{(k)}, \ldots, \tau_N^{(k)}\right]^t$, yielding

$$\mathbf{A}'_{(k)} \boldsymbol{\delta\tau}_{(k)} + \mathbf{A}\left(\boldsymbol{\tau}_{(k)}\right) = \mathbf{y} \tag{4}$$

where symbol $\mathbf{A}'_{(k)}$ indicates the Fréchet derivative of $\mathbf{A}$ at $\boldsymbol{\tau}_{(k)}$, and $\boldsymbol{\delta\tau}_{(k)}$ is the linearized problem unknown. The truncated Landweber method in variable exponent Lebesgue spaces (inner loop) is adopted to find $\boldsymbol{\delta\tau}_{(k)}$ [16], in which the exponent function $\mathbf{p}_{(k)}$ is defined as

$$\mathbf{p}_{(k)} = \begin{bmatrix} \Delta p \left(\left| \tau_1^{(k)} \right| / \max_n \left| \tau_n^{(k)} \right| - 1 \right) + 2 \\ \vdots \\ \Delta p \left(\left| \tau_N^{(k)} \right| / \max_n \left| \tau_n^{(k)} \right| - 1 \right) + 2 \end{bmatrix} \tag{5}$$

with $0 \leq \Delta p < 1$. This choice allows adaptively placing higher exponent values where targets are detected and lower values outside. Once $\boldsymbol{\delta\tau}_{(k)}$ is found, the iterative solution update follows as $\boldsymbol{\tau}_{(k+1)} = \boldsymbol{\tau}_{(k)} + \boldsymbol{\delta\tau}_{(k)}$ until convergence is reached.

3. Results of Numerical Tests

The method has been evaluated in a numerically simulated environment, where a set of $I = 20$ antennas modeled as open waveguides is located in a square of side $l_S = 22$ cm. The waveguides (width $a = 1.6$ cm and length $d = 2.5$ cm) are filled with a material of dielectric permittivity $\varepsilon_{\text{wg}}^* = 4\varepsilon_0$. A target with a cylindrical shape and square cross-section of side $l_T = 2.5$ cm, centered at $\mathbf{r}_T = (-2.4,\ 2.6)$ cm and characterized by $\varepsilon_{\text{tar}}^* = (2 - j0.3)\varepsilon_0$, is considered. In addition, a cylindrical metallic target with a circular cross-section (modeled as a perfect electric conductor) is centered at $\mathbf{r}_M = (-1.5,\ 4.5)$ cm. The configuration has been simulated to compute the incident and total S parameters at frequency $f = \omega/2\pi = 6$ GHz. Two cases have been analyzed: at first, a priori information concerning the size and position of the metallic target is included in the model; second, no a priori information about the metallic object is assumed known.

The simulation domain is discretized with a frontal Delaunay algorithm through Gmsh [17] and a maximum edge of size $e_{\text{wg}} = 0.1$ cm at antenna ports and $e_S = 0.2$ cm elsewhere. The fundamental mode at waveguide ports is considered, and absorbing boundary conditions are enforced by contouring the computational domain with a perfectly matched anisotropic absorber [15]. Moreover, for each view, $L = 3$ is considered. Total S parameters are corrupted with a 3% multiplicative Gaussian noise [18]. The inversion method parameters have been set as follows: maximum number of Landweber and IN iterations $N_{\text{it}} = 50$; threshold on the residual relative variation $r = 0.1$ %; and range of the exponent function $\Delta p = 0.5$. The square region of interest for the inversion has side $l_R = 14$ cm and is partitioned into triangular elements with $e_{\text{wg}} = 0.1$ cm at antenna ports and $e_S = 0.4$ cm elsewhere.

The method has been quantitatively evaluated by means of the relative reconstruction error on τ in the background (R_{bg}) and in the region that includes the dielectric target (R_{tar}):

$$e_{\{\text{bg,tar}\}} = \frac{1}{N_{\{\text{bg,tar}\}}} \sum_{n \in \{R_{\text{bg}}, R_{\text{tar}}\}} \frac{|\tau_n - \widetilde{\tau_n}|}{|\widetilde{\tau_n} + 1|} \tag{6}$$

with $N_{\{\text{bg,tar}\}}$ the number of elements in $\{R_{\text{bg}}, R_{\text{tar}}\}$, τ_n the reconstructed contrast function in the nth mesh element, and $\widetilde{\tau_n}$ its reference value.

The first set of numerical simulations analyzes a variation in the metallic target's size. In particular, in case 1, the radius of circular cross-section is $r_M = 0.3$ cm, case 2 has $r_M = 0.6$ cm, and case 3 is $r_M = 1.2$ cm. The reconstructed distributions of the complex relative dielectric permittivity inside R for the previously mentioned three cases, obtained with a priori knowledge of the metallic target, are reported in Figure 1. For all configurations, a good reconstruction is achieved, and the dielectric target is well visible and correctly localized with an adequate estimation of its shape. The average reconstruction of the permittivity is close to its actual value. By increasing the size of the metallic target, a slight worsening in the background reconstruction can be noticed.

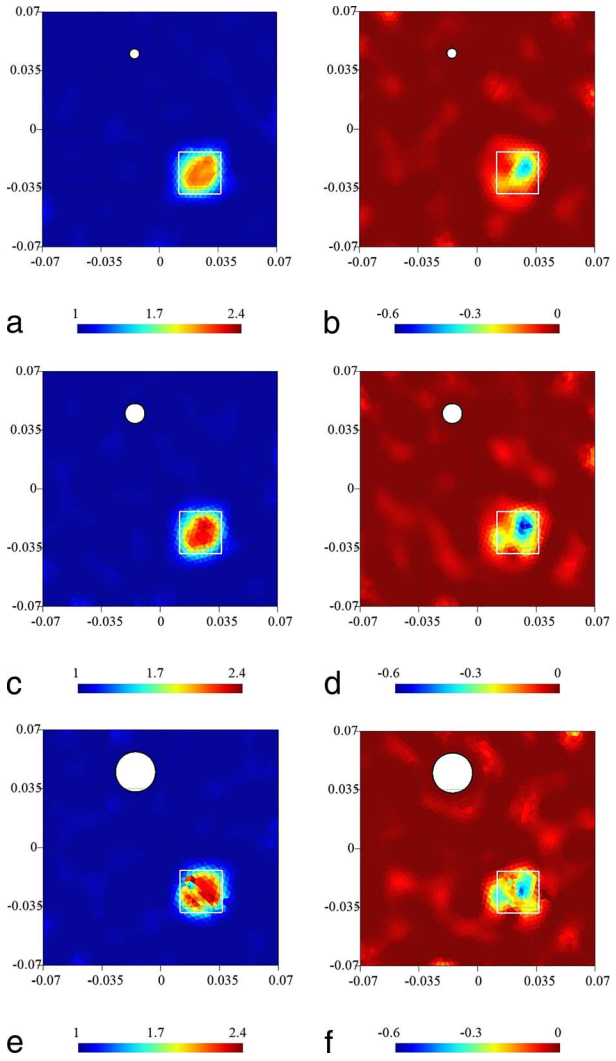

Figure 1. Reconstructed distributions of the relative dielectric permittivity with a priori knowledge of the metallic target. Case 1 (a) real and (b) imaginary part; case 2 (c) real and (d) imaginary part; and case 3 (e) real and (f) imaginary part.

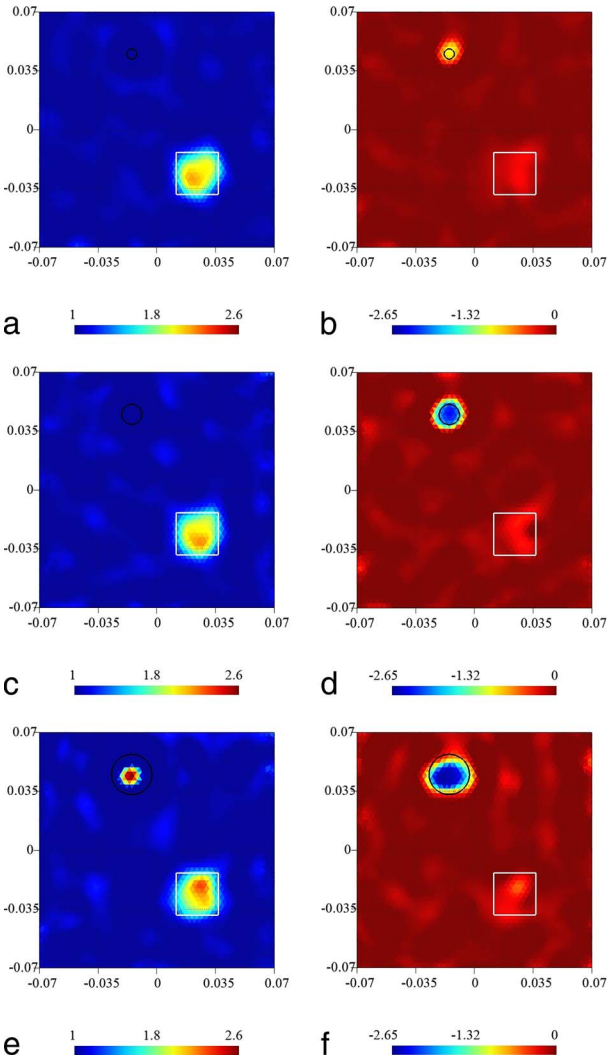

Figure 2. Reconstructed distributions of the relative dielectric permittivity without a priori knowledge of the metallic target. Case 1 (a) real and (b) imaginary part; case 2 (c) real and (d) imaginary part; and case 3 (e) real and (f) imaginary part.

In Figure 2, results obtained with no a priori knowledge of the metallic target are reported. For all cases, it is possible to identify both dielectric and metallic targets. The presence of the metallic target is evident from the imaginary part of the permittivity, and overall, its different dimensions are correctly identified (case 1 in Figure 2b, case 2 in Figure 2d, and case 3 in Figure 2f). However, a less accurate reconstruction of the dielectric target is obtained, especially in the imaginary part of the relative dielectric permittivity. Moreover, by increasing the metallic target dimension, a progressive worsening in the reconstruction can be observed: this is due to the increasing interactions between the metallic structure and the dielectric object.

Relative reconstruction errors for the analyzed configurations are reported in Table 1. By comparing the errors, it is evident that, as expected, the knowledge of the metallic target allows a better reconstruction of both background and dielectric properties of the other object, especially for greater metallic target sizes. When the metallic structure is included in the model, the error in the background slightly increases by increasing the metallic target size and the dielectric target reconstruction accuracy is basically stable. Conversely, when no a

Table 1. Relative reconstruction errors in the background and inside the dielectric target region with a single metallic target

Case	Background error e_{bg}	Target error e_{tar}
Unknown metallic target		
1	0.066	0.258
2	0.098	0.420
3	0.181	0.568
Known metallic target		
1	0.025	0.138
2	0.030	0.140
3	0.033	0.140

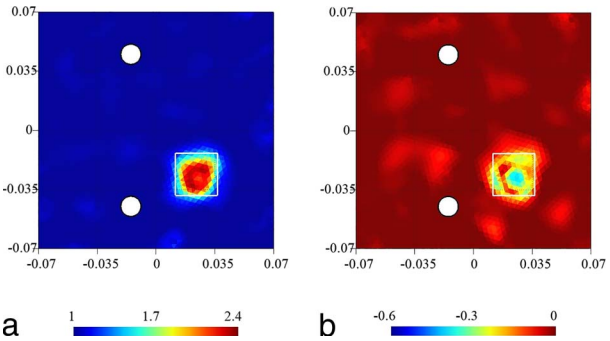

Figure 3. Reconstructed distributions of the relative dielectric permittivity with two metallic targets and a priori knowledge of their presence: (a) real and (b) imaginary part.

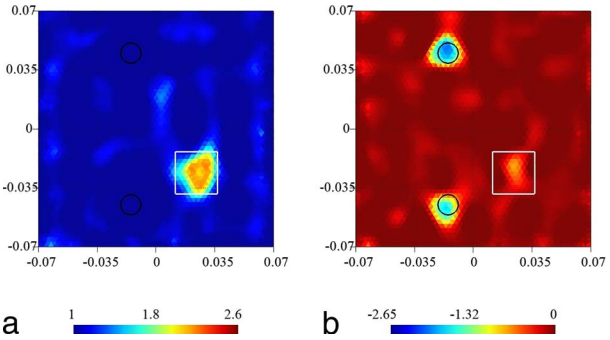

Figure 4. Reconstructed distributions of the relative dielectric permittivity with two metallic targets and without a priori knowledge of their presence: (a) real and (b) imaginary part.

priori information is supposed to be available, the error increases significantly together with the target size. Nevertheless, even without a prior knowledge of the presence of the metallic structure, all targets can still be quite correctly identified.

A second test has been performed by increasing the number of metallic targets. A second one has been introduced in the configuration of case 2, centered at $\mathbf{r}_T = (-1.5, \ -4.5)$ cm. The obtained reconstructions are reported in Figures 3 and 4, with and without a priori knowledge of the metallic cylinders, respectively. In Table 2, the reconstruction errors are shown. As can be noted in Figure 3, a good estimation of the properties of the dielectric target is achieved without significant artifacts in the background. A slightly worse reconstruction is presented in Figure 4, which corresponds to higher reconstruction errors (Table 2). Nevertheless, all targets are correctly localized and identified even in this more challenging case.

Table 2. Relative reconstruction errors in the background and inside the dielectric target region with two metallic targets

	Number of metallic targets	Background error e_{bg}	Target error e_{tar}
Unknown metallic targets	2	0.193	0.632
Known metallic targets	2	0.031	0.152

4. Conclusions

A microwave imaging approach based on variable exponent Lebesgue space inversion with an FE-based formulation is applied in this article to the challenging case of reconstructing mixed configurations with both metallic and dielectric targets. The method has been assessed through a set of numerical simulations, analyzing the effect of different dimensions and numbers of metallic targets present in the region of interest. Promising results have been obtained even without an a priori knowledge of the presence of metallic inclusions. The obtained results stimulate the application of the proposed technique to various real-world scenarios (e.g., buried object detection or medical imaging), as well as its generalization to the three-dimensional case.

5. References

1. M. Pastorino and A. Randazzo, *Microwave Imaging Methods and Applications*, Boston, Artech House, 2018.
2. R. Pierri, A. Liseno, R. Solimene, and F. Soldovieri, "Beyond Physical Optics SVD Shape Reconstruction of Metallic Cylinders," *IEEE Transactions on Antennas and Propagation*, **54**, 2, February 2006, pp. 655-665.
3. S. Meschino, L. Pajewski, M. Pastorino, A. Randazzo, and G. Schettini, "Detection of Subsurface Metallic Utilities by Means of a SAP Technique: Comparing MUSIC- and SVM-Based Approaches," *Journal of Applied Geophysics*, **97**, October 2013, pp. 60-68.
4. A. Ali, M. E. Badawe, and O. M. Ramahi, "Microwave Imaging of Subsurface Flaws in Coated Metallic Structures Using Complementary Split-Ring Resonators," *IEEE Sensors Journal*, **16**, 18, September 2016, pp. 6890-6898.
5. S. Sun, B. J. Kooij, and A. G. Yarovoy, "A Linear Model for Microwave Imaging of Highly Conductive Scatterers," *IEEE Transactions on Microwave Theory and Techniques*, **66**, 3, March 2018, pp. 1149-1164.
6. L. Crocco, L. Di Donato, I. Catapano, and T. Isernia, "An Improved Simple Method for Imaging the Shape of Complex Targets," *IEEE Transactions on Antennas and Propagation*, **61**, 2, February 2013, pp. 843-851.
7. M. Fallahpour, J. T. Case, M. T. Ghasr, and R. Zoughi, "Piecewise and Wiener Filter-Based SAR Techniques for Monostatic Microwave Imaging of Layered Structures," *IEEE Transactions on Antennas and Propagation*, **62**, 1, January 2014, pp. 282-294.
8. M. R. Ramzi, M. Abou-Khousa, and I. Prayudi, "Near-Field Microwave Imaging Using Open-Ended Circular Waveguide Probes," *IEEE Sensors Journal*, **17**, 8, April 2017, pp. 2359-2366.
9. M. Maffongelli, R. Monleone, M. Pastorino, S. Poretti, A. Randazzo, et al., "Reconstruction of Metallic Inclusions Inside Dielectric Targets by Means of a Microwave Tomographic System," *IEEE Microwave and Wireless Components Letters*, **22**, 7, 2012, pp. 378-380.
10. A. Fedeli, V. Schenone, A. Randazzo, M. Pastorino, T. Henriksson, et al., "Nonlinear S-Parameters Inversion for Stroke Imaging," *IEEE Transactions on Microwave Theory and Techniques*, **69**, 3, March 2021, pp. 1760-1771.
11. P. Mojabi and J. LoVetri, "A Prescaled Multiplicative Regularized Gauss-Newton Inversion," *IEEE Transac-*

tions on Antennas and Propagation, **59**, 8, August 2011, pp. 2954-2963.

12. A. Abubakar, T. M. Habashy, G. Pan, and M.-K. Li, "Application of the Multiplicative Regularized Gauss-Newton Algorithm for Three-Dimensional Microwave Imaging," *IEEE Transactions on Antennas and Propagation*, **60**, 5, May 2012, pp. 2431-2441.
13. A. Fedeli, C. Estatico, A. Randazzo, and M. Pastorino, "Multifrequency Microwave Tomography in Lebesgue Spaces with Nonconstant Exponents," *URSI Radio Science Letters*, **2**, 2020, pp. 1-4.
14. N. K. Nikolova, *Introduction to Microwave Imaging*, Cambridge, UK, Cambridge University Press, 2017.
15. G. Pelosi, R. Coccioli, and S. Selleri, *Quick Finite Elements for Electromagnetic Waves*, 2nd Ed., Norwood, MA, Artech House, 2009.
16. C. Estatico, A. Fedeli, M. Pastorino, and A. Randazzo, "Quantitative Microwave Imaging Method in Lebesgue Spaces with Nonconstant Exponents," *IEEE Transactions on Antennas and Propagation*, **66**, 12, December 2018, pp. 7282-7294.
17. C. Geuzaine and J.-F. Remacle, "Gmsh: A 3-D finite Element Mesh Generator With Built-In Pre- and Post-Processing Facilities," *International Journal for Numerical Methods in Engineering*, **79**, 11, September 2009, pp. 1309-1331.
18. P.-H. Tournier, M. Bonazzoli, V. Dolean, F. Rapetti, F. Hecht, et al., "Numerical Modeling and High-Speed Parallel Computing: New Perspectives on Tomographic Microwave Imaging for Brain Stroke Detection and Monitoring," *IEEE Antennas and Propagation Magazine*, **59**, 5, October 2017, pp. 98-110.